Pseudo-full-waveform inversion of borehole GPR data using stochastic tomography

Erwan Gloaguen[1], Bernard Giroux[2], Denis Marcotte[2], and Roussos Dimitrakopoulos[3]

ABSTRACT

Electromagnetic full-waveform tomography is computer intensive and requires good knowledge of antenna characteristics and ground coupling. As a result, ground-penetrating-radar tomography usually uses only the first wavelet's arrival time and amplitude data. We propose to improve the classical approach by inverting multiple slowness and attenuation fields using stochastic tomography. To do so, we model the slowness and attenuation covariance functions to generate geostatistical simulations that are conditional to the arrival times, amplitudes, slowness, and attenuation observed along boreholes. We combine slowness and attenuation fields to compute conductivity and permittivity fields from which we model synthetic radar traces using a finite-difference time-domain full-waveform algorithm. Modeled traces that best match the measured ones correspond to the computed conductivity and permittivity fields that correlate best with the true physical properties of the ground. We apply the method to a synthetic example with known electric properties. We show that a combination of stochastic tomography and full-waveform modeling allows a better selection of permittivity fields close to the reference field, at a reasonable computing cost.

INTRODUCTION

Ray-based ground-penetrating-radar (GPR) tomography is a well-known imaging technique that allows one to compute the slowness and attenuation of an electromagnetic (EM) wave within a medium. With this method we use the traveltime and amplitude of the wave traveling directly from a transmitter located in a hole, to a receiver in another hole (Vasco et al., 1997; Lane et al., 1998; Belle-

fleur et al., 2000). Aside from the optical frequency approximation, the most important limitation of ray-based tomography is that it takes into account only the first-arrival wavelet parameters, i.e., the wavelet's traveltime and amplitude. Ray-based tomography totally neglects secondary events such as reflected or refracted waves. Although full-waveform tomography takes these events into account (Cai et al., 1996; Alumbaugh and Newmann, 2000), the difficulty in adequately taking into account antenna characteristics (Giroux and Chouteau, 2006), along with the method's high computational cost, implies a need for alternative methods (Luo and Schuster, 1991).

To overcome the computational burden of full-waveform tomography, we propose a two-step method in which ray-based stochastic simulation (Gloaguen et al., 2003) is used first to generate several statistically equivalent realizations of slowness and attenuation fields, thereby showing the variability that can be expected from the estimated covariance model. A complete review of stochastic tomography, including comparison with classical conjugate-gradient-based (LSQR) and projection-based (SIRT) algorithms, can be found in Gloaguen et al. (2005). Once the slowness and attenuation estimates are obtained, electric conductivity and permittivity are computed assuming a nondispersive medium combining all slowness and attenuation simulations (Topp et al., 1980; Hollender, 1999; Tronicke et al., 2004; Day-Lewis et al., 2005; Hyndman and Tronicke, 2005; Lesmes and Friedman, 2005). All the calculated physical property fields are then used to generate pseudo-GPR traces through finite-difference time-domain (FDTD) full-waveform modeling. Crosscorrelation between computed and observed traces is calculated. For each trace, the maximum correlation delay time is obtained as well as the maximum correlation value itself. Finally, for each simulated pseudotrace data set, the delay times and the maximum correlation values are averaged. The simulated fields showing the smallest discrepancy between observed and computed traces are considered to be the fields that best resemble the real one.

Furthermore, when one is using borehole reflection surveys or electromagnetic logging tools, it is possible to measure velocity and/or attenuation along the holes. The stochastic simulation method allows one to include these additional data and to fit them exactly. This leads to a dramatic increase in the accuracy of the solution and to a decrease of the uncertainty regarding the slowness and attenuation estimates (Gloaguen et al., 2005).

In the following section, the GPR technique and the theory of GPR tomography are briefly introduced and the geostatistical approach is described. The performance of the proposed method is then examined with a synthetic model.

GPR TOMOGRAPHY THEORY

In this section we show how the electric property of a material can be inferred from EM wave velocity and attenuation. EM theory at radio frequency is briefly discussed, after which slowness and attenuation ray-based tomographies are presented.

EM wave theory

The far-field amplitude of an EM wave that is emitted by a dipole and is propagating through a homogeneous medium at a distance r is given by (Balanis, 1989):

$$A_r = A_0 e^{-\alpha r} e^{i(\omega t - \beta r)}, \qquad (1)$$

where A_r is the wave amplitude at distance r from the transmitter, A_0 is the amplitude at the transmitter, α is the attenuation expressed in Np/m, ω is the angular frequency, t is the time taken by the wave to travel from the source to the receiver, and β is the phase constant in rad/m.

For lossy and nondispersive media with magnetic permeability of the free space μ_0, β and α are given by

$$\begin{cases} \alpha = \dfrac{\omega}{c} \left[\dfrac{1}{2} \left(\sqrt{\epsilon_r^2 + \left(\dfrac{\sigma}{\omega \epsilon_0} \right)^2} - \epsilon_r \right) \right]^{1/2} \\[4mm] \beta = \dfrac{\omega}{c} \left[\dfrac{1}{2} \left(\sqrt{\epsilon_r^2 + \left(\dfrac{\sigma}{\omega \epsilon_0} \right)^2} + \epsilon_r \right) \right]^{1/2} \end{cases}, \qquad (2)$$

where ϵ_r is the real relative permittivity or dielectric constant of the medium, ϵ_0 is the permittivity of free space, c is the EM velocity in free space with $c = 1/\epsilon_0 \mu_0$, and σ is the real electric conductivity of the medium. In addition, there is a relation between the velocity of a radar wave v and its phase β:

$$v = \frac{\omega}{\beta}. \qquad (3)$$

By a combination of relations 2 and 3, the permittivity and the conductivity can be represented in terms of velocity and attenuation:

$$\begin{cases} \epsilon_r = \dfrac{\left(\dfrac{1}{v} \right)^2 - \left(\dfrac{\alpha}{\omega} \right)^2}{\mu_0 \epsilon_0} \\[6mm] \sigma = \dfrac{2\alpha}{\mu_0 v} \end{cases}. \qquad (4)$$

These physical properties make it possible to characterize a given material and to estimate the porosity and water content of nondisper-

sive materials using empirical relationships such as the Topp relation, or in situ calibration (Topp et al., 1980; Gloaguen et al., 2001; Tronicke et al., 2002, 2004; Hyndman and Tronicke, 2005).

Slowness tomography

Several GPR full-waveform tomography techniques exist (Cai et al., 1996; Alumbaugh and Newmann, 2000), but each has its limitations. Full-waveform inversion, a typical nonlinear problem, implies iterative computation of forward modeling several times, which is a huge computational burden. For example, full-waveform modeling of ten thousand traces on a 3.2-million-cell model can take as much as 72 hours on a cluster of a subset of 800 Pentium IV processors. Such computational costs motivate the use of ray approximation. If one assumes infinite frequency, a ray can be defined as the curve that connects a transmitter to a receiver and lies perpendicular to the wavefront (Berryman, 1991). For EM waves, the ray geometry depends on contrasts of the electric properties, and, thus, on the velocity contrasts as stated by the Snell-Descartes law. In ray-based tomography, the field is discretized as a set of cells. For each transmitter-receiver pair, the length of each segment of raypath that crosses a cell is computed. All the segment lengths are organized in a (sparse) matrix **L**, called the raypath matrix, which describes the geometry of the rays. **L** is of the size n_t observed times by n_p cells (of constant slowness). If the ray assumption is acceptable, equation 5 represents the linear relation between the traveltime vector **t** and the slowness vector **s**:

$$\mathbf{Ls} = \mathbf{t}. \qquad (5)$$

Equation 5 represents the forward modeling of the traveltime. The slowness field must be estimated by the inversion of equation 5. Unfortunately, GPR borehole tomography is a prime example of an ill-posed problem (Berryman, 1991), so **L** is not directly invertible. Note that the raypath matrix **L** is unknown because it depends on the velocity contrasts. **L** is obtained iteratively by first assuming straight rays (a homogeneous medium) and getting an initial solution of velocity by cokriging. Using the Snell-Descartes law, a new **L** is calculated on the basis of the cokriged velocity field. Cokriging and raypath updating are repeated until the variation between two successive cokriged velocity solutions becomes negligible.

Attenuation tomography

The relation between the amplitude of the emitted pulse at the transmitter A_0 and the measured amplitude A_r of a plane wave traveling through a homogeneous medium with a raypath of length r between the transmitter and the receiver can be written (Zhou and Fullagar, 2001) as

$$A_r = A_0 e^{-\int_0^r \alpha(l) dl}, \qquad (6)$$

where $\alpha(l)$ is the attenuation of the cell located at distance l from the source. The measured amplitudes have to be corrected for the radiation pattern of the antennas and the geometric spreading of the wave (Holliger and Bergmann, 2002).

Then, equation 6 becomes

$$A_r = \frac{A_0 e^{-\int_0^r \alpha(l)dl} \Gamma_e(\theta) \Gamma_r(\theta)}{\int_0^r dl}, \qquad (7)$$

where $1/\int_0^r dl$ is the geometric spreading, Γ_e is the correcting function for the transmitting antenna as a function of angle θ_e, and Γ_r is the correcting function of the receiving antenna as a function of angle θ_r. The terms A_0, Γ_e, and Γ_r, cannot be known easily and have to be approximated. This makes amplitude tomography somewhat less robust than slowness tomography. A_0 is approximated by linear regression of the picked amplitudes and transmitter-receiver separation distances. The angles θ_e and θ_r are defined in Figure 1. For bipolar antennas located in the same plane and for homogeneous media, the antenna radiation patterns Γ can be approximated by sinusoid functions (Zhou and Fullagar, 2001).

For a given transmitter-receiver pair i, the discrete form of equation 7 becomes

$$A_i = \frac{A_0 e^{-\sum_{j=1}^{Nj} \alpha_j l_{ij}} \sin(\theta_e)\sin(\theta_r)}{\sum_{j=1}^{Nj} l_{ij}}, \qquad (8)$$

where j is the cell number and Nj is the number of cells.

Rearranging and taking the natural logarithm of equation 8 leads to

$$\sum_{j=1}^{Nj} \alpha_j l_{ij} = ln(A_0) - ln\left(\frac{A_i r}{\sin(\theta_e)\sin(\theta_r)}\right). \qquad (9)$$

The raypaths are computed during slowness tomography; A_i is the measured amplitude, A_0 is estimated, and angles θ_e and θ_r are computed knowing the raypaths and the hole geometries. Equation 9 leads to a linear equation:

$$L\alpha = \mathbf{A}, \qquad (10)$$

where the ith value of vector $\mathbf{A}$ is given by $A_i = ln(A_0) - ln$ $(A_i r/\sin(\theta_e)\sin(\theta_r))$.

As is shown in the next section, this linear system is solved by using the same procedure as that used for the slowness tomography.

STOCHASTIC TOMOGRAPHY

In this section, the stochastic tomography method based on ray approximation is briefly presented. The flowchart of the method is shown in dashed lines in Figure 2. Theoretical and implementational details can be found in Gloaguen et al. (2005) and Giroux et al. (2007). This algorithm solves both velocity and attenuation tomographies, which are two linearized problems. Because the algorithm remains the same and because slowness tomography needs to be performed prior to attenuation tomography (box 4 in Figure 2), the notation used in the following sections is that of slowness tomography.

Slowness covariance modeling

The key step of stochastic linear inverse theory comprises the modeling of the covariance of the parameter (here, the slowness) and

calculation of the cross-covariance between data (here, the traveltimes) and parameter (Franklin, 1970; Kitanidis, 1995; Asli et al., 2000). This step is represented in box 1 in Figure 2. In this section, the proposed covariance modeling technique is presented and the assumption on noise distribution is discussed.

As was shown previously, $\mathbf{s}$ and $\mathbf{t}$ are related linearly (equation 5). As a consequence, slowness and traveltime covariance matrices also are related linearly:

$$\mathbf{C_t} = \mathbf{LC_s L}^T + \mathbf{C_0}, \qquad (11)$$

where $\mathbf{C_t}$ is the $n_t \times n_t$ traveltime covariance matrix, $\mathbf{C_s}$ is the $n_p \times n_p$ slowness covariance matrix, and $\mathbf{C_0}$ is the $n_t \times n_t$ traveltime-error covariance matrix. This error covariance matrix combines the effects of the picking error and model discretization used to represent the real slowness field. These errors usually are modeled as a nugget effect (white noise). Note that only Gaussian noise with constant variance $\mathbf{C_0}$ is taken into consideration. In a real data acquisition, multiple sources of error exist: unknown or inaccurately measured borehole deviations and offsets, errors in assumed source-receiver radiation patterns, inaccurate "zero times" in trace recording, and time-varying output power for attenuation tomography. These errors either have to be filtered out prior to analysis or the error matrix has to be known a priori or assumed to have a specific structure. On the other hand, the $\mathbf{LC_s L}^T$ matrix represents the covariance component in traveltimes because of the spatial structure of the slowness and the raypath propagation. Also, it is easy to verify that, because of the linearity of equation 5, the cross-covariance between traveltimes and slowness is given by $\mathbf{C_{ts}} = \mathbf{LC_s}$.

The slowness covariance matrix $\mathbf{C_s}$ is computed by specifying a model function or a combination of model functions, with a given range a corresponding to the distance after which slowness is uncorrelated, and with sill C representing the variance of the slowness (box 1 in Figure 2). The model function parameters a and C are estimated using an iterative search in the low dimension of the function's parameter space, by comparing theoretical traveltime covariances with observed traveltime (experimental) covariances (equation 11). Good correspondence between theoretical and experimental covariances implies that the data support the choice of parameters of the slowness covariance function and the function itself (Gloaguen et al., 2005).
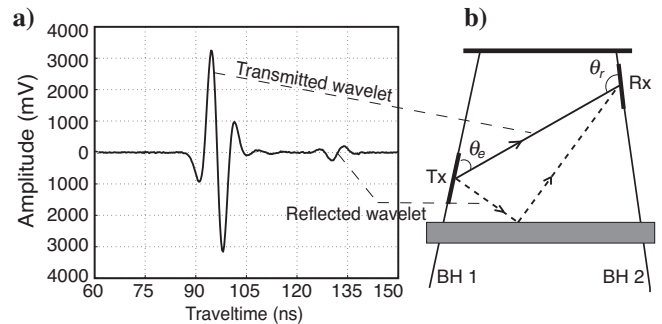

Figure 1. (a) Example of a synthetic trace, showing the transmitted wavelet (90 to 105 ns) and a reflected wavelet (between 125 and 135 ns). (b) Corresponding ground model, showing angles allowing one to correct the amplitude for the radiation patterns of the antennas (θ_e is the angle between the transmitting antenna and the outgoing ray, and θ_r is the angle between the receiving antenna and the incoming ray). Tx and Rx are the transmitter and receiver locations, respectively, in boreholes BH1 and BH2.

Cokriging and geostatistical simulation

Once the parameters of the slowness covariance function have been estimated, the slowness field is cokriged using the arrival times and any available slowness data (box 2 in Figure 2). By construction, cokriging gives a smooth estimate of the slowness field, thereby allowing numerical stability in the curved ray computation. However, the cokriged estimate does not necessarily reproduce the modeled covariance function and does not realistically represent the spatial heterogeneity of the ground. It may be desirable and informative to obtain various equiprobable solutions that show the kind of variability one can expect from the covariance model that is adopted and constrained by the observed traveltimes. Within the geostatistical framework, this can be done by using stochastic simulation algorithms (box 3 in Figure 2). Among the various geostatistical simulation methods (Chilès and Delfiner, 1999), the fast Fourier transform–moving average (FFT-MA) algorithm (Le Ravalec et al., 2000) has been retained for its rapidity. The FFT-MA algorithm generates nonconditional Gaussian stationary processes on regular grids, thereby implying that observed traveltimes are not honored. Postconditioning (Chilès and Delfiner, 1999) is done using cokriging weights computed at box 2 in Figure 2. This also motivates the choice of the FFT-MA algorithm. Finally, each conditional simulation has the desired covariance and any additional slowness constraints are fitted exactly. The computed traveltimes on each conditional simulation of a slowness field will not be exactly equal to the

observed traveltimes because the true raypaths are not the same as the raypaths used for the postconditioning. Again, this is a manifestation of the nonlinearity between raypath and slowness field. In this case, a nugget effect is present in observed traveltimes, and the computed times depart from the observed times by an amount compatible with the level of error described by this nugget effect.

PSEUDO-FULL-WAVEFORM TOMOGRAPHY

In this section, we describe the pseudo-full-waveform tomography. The flowchart of the method is represented in full lines and boxes in Figure 2.

Gound-penetrating-radar stochastic tomography provides several different slowness and attenuation fields that share the same variogram and histogram and that honor the picked amplitudes and traveltimes with the same accuracy. Under the assumption of a nondispersive medium, permittivity and conductivity fields are calculated by combining attenuation and slowness fields using relation 4 (box 5 in Figure 2). To select the physical-property fields that best correlate with the real permittivity and conductivity fields, we propose to compute pseudotraces at the same location as the observed ones (box 6 in Figure 2). The pseudotraces do not just contain the picked traveltimes and amplitudes of the first-arrival wavelet. They also represent the complete first-arrival wavelet and also possible secondary events, such as reflections or refractions. The pseudotraces associated with the simulated permittivity and conductivity fields that best match the observed traces are expected to have the highest correlation with the real physical-property fields (box 7 in Figure 2).

First, the full-waveform modeling algorithm is briefly presented, and then the method for comparing observed and pseudotraces is described.

Description of the full-waveform FDTD algorithm

An FDTD implementation of Maxwell's equations in cylindrical coordinates was developed to model the GPR traces. Following Holliger and Bergmann (2002), this implementation relies on rotational symmetry with respect to the boring axis to transform the 3D equations to 2D. Our implementation is fourth-order in space and also incorporates an optional dielectric relaxation term (as formulated by Carcione and Schoenberg [2000]). A perfectly matched layer implementation in complex coordinates (Chew et al., 1997) is used to eliminate the reflections at the grid borders.

Observed versus computed traces

Once the traces have been modeled, observed and simulated trace sets are compared. There are two parameters of interest: the time shift, which is mainly related to the permittivity field, and the amplitude difference, which is mainly affected by the conductivity.
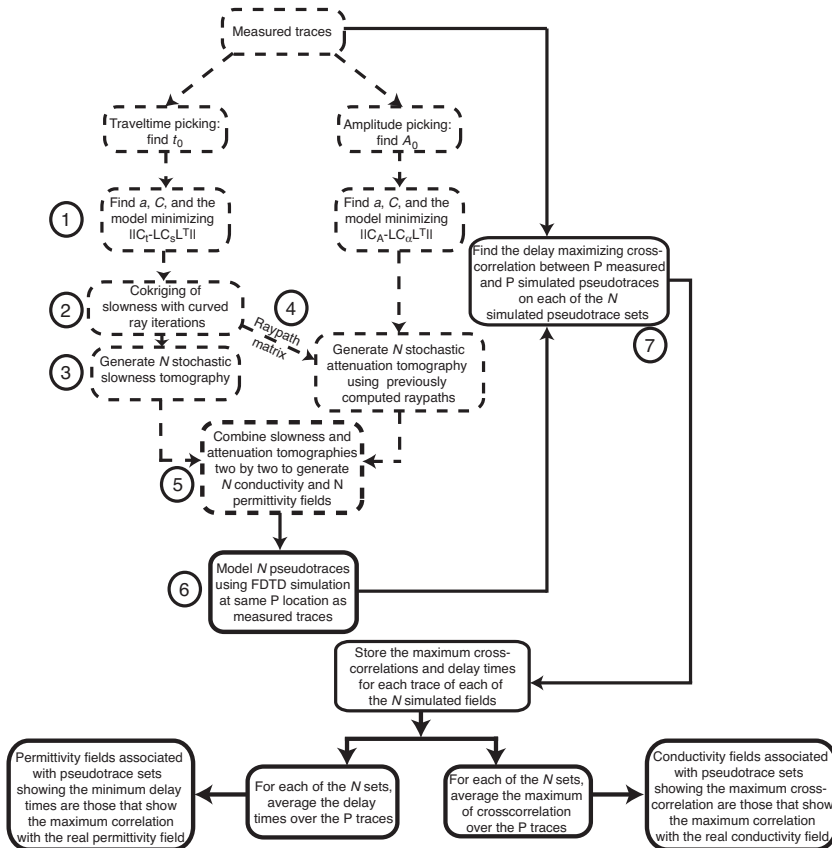

Figure 2. Flowchart of the proposed method. The dashed lines and boxes represent the stochastic tomography method (Gloaguen et al., 2005). The full lines and boxes pertain to the new contribution.

A common way of evaluating the misfit between two sets of GPR traces is to compute the crosscorrelation between each set of traces (Yilmaz, 2001). The crosscorrelation between two complex traces, $t1$ and $t2$, is given by the following general equation:

$$c_{t1,t2}(\tau) = \int_{-\infty}^{+\infty} t1(s)t2^{\star}(s - \tau)ds, \qquad (12)$$

where τ is the delay and $t2^{\star}$ is the complex conjugate of $t2$. The τ value that maximizes the crosscorrelation gives the delay. The most accurately computed trace set maximizes the crosscorrelation and minimizes the delay.

A SYNTHETIC MODEL CASE STUDY

In this section, the method is tested using a synthetic model of the electric properties of the ground. Figure 3 shows the synthetic electric-conductivity field, and Figure 4 shows the synthetic dieletric-constant, or permittivity field (hereafter called *reference fields*). The mean and spatial distribution of the electric properties correspond to a sand having moisture content varying from 3% to 30%. FDTD full-waveform modeling is computed using these two petrophysical models to generate pseudomeasured GPR traces (hereafter called *reference traces*). To obtain enough accuracy and to respect stability conditions, the modeling domain is sampled every centimeter horizontally and vertically and the time step is 0.01 ns. The modeling domain is divided into three adjacent panels, each comprising 60 transmitters and 60 receivers, thus leading to 10,800 traces to model. Gaussian noise of 3% is added to all the traces to mimic a real acquisition. Figure 5 shows an example of a reference trace for which the transmitter is located in the first hole (a distance of 1 m) at a depth of 2 m, and the receiver is located in the second hole (a distance of 7 m) at a depth of 7.75 m.

Vertical profiles of permittivity and conductivity along the holes are extracted from the reference models to provide well-logging data. The sampling interval along the holes is 20 cm.
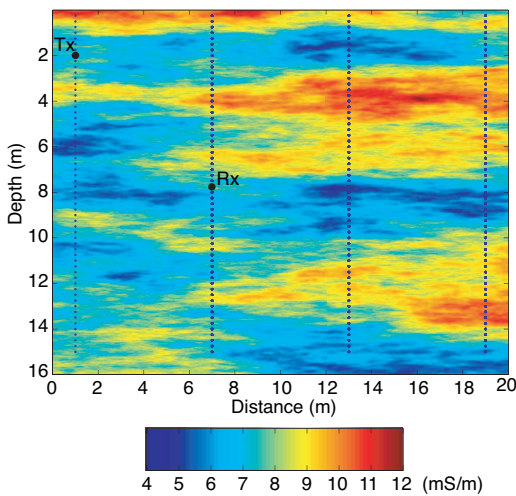
Figure 3. Synthetic electric-conductivity field. Dashed lines indicate borehole locations. Particular transmitter (Tx) and receiver (Rx) locations corresponding to the trace shown in Figure 5 are marked.

Tomography on synthetic data

First-arrival picking was done manually on each reference trace. Using borehole logging data acquired along the holes and traveltime data, an anisotropic slowness covariance model is fitted using equation 11. The fitted model is spherical, with ranges of 9.5 m perpendicular to boreholes and 2.2 m along the holes. The variance is 0.4 $(ns/m)^2$. Using the modeled covariances, the logging data, and the traveltimes, 128 slowness simulations were generated. Two curved ray iterations were necessary to honor the data. Cokriged models are inherently smoother than simulated models. Hence, we choose to compute the curved raypaths using the cokriged slowness model to avoid numerical artifacts during the ray-tracing procedure. This choice is also supported by the fact that the radar wavelength is larg-
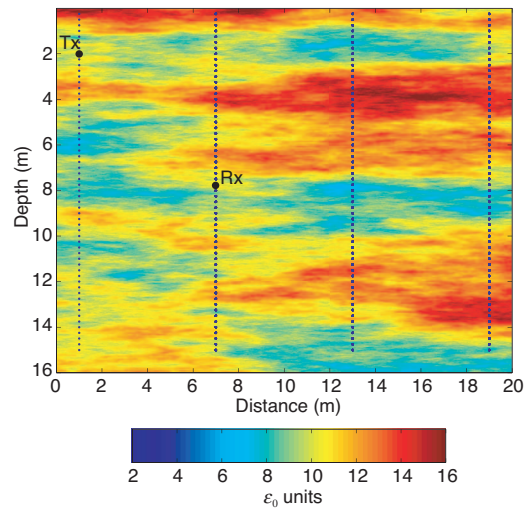
Figure 4. Synthetic dielectric-constant field. Dashed lines indicate borehole locations. Particular transmitter (Tx) and receiver (Rx) locations corresponding to the trace shown in Figure 5 are marked.
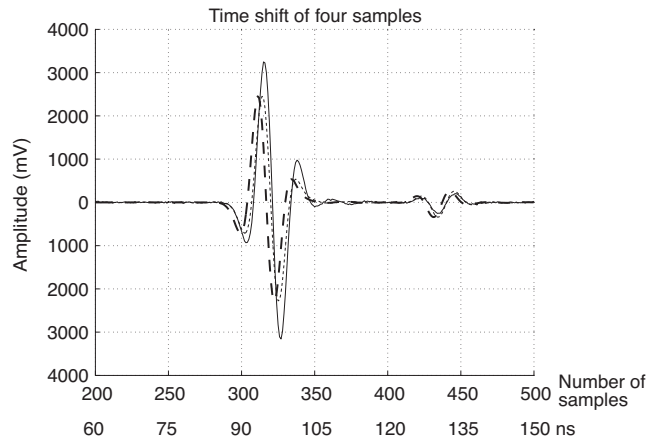
Figure 5. Example of a measured (reference) trace (continuous line), best-fit simulated trace (dashed line), and the same simulated trace shifted by the delay of maximum correlation (dotted line). The first-arrival wavelet interval is between 290 and 350 samples, corresponding to an interval of 87 to 105 ns, and a secondary event occurs between 425 and 450 samples, corresponding to an interval of 127 to 135 ns. The time step is 0.3 ns per sample. Tx is located in the first hole (1 m along the x-axis) at a 2-m depth, and the receiver (Rx) is at 7.75 m in the second hole (7 m along the x-axis).

er than the grid size, and as a consequence the propagation of the radar wave is weakly affected by local variations. Finally, this approach is computationally more efficient because the ray-tracing procedure is carried out only once every iteration.

Figure 6 shows four randomly selected slowness simulations from among the set of 128. Because of restrictions in computational resources, the tomographic calculations are carried out on a coarser grid than that used for FDTD modeling: 30 by 30 cm versus 1 by 1 cm, respectively. As a result of the conditioning, all the simulated slowness fields share the same global features, that is, alternate layers of high and low velocity. However, moderate local variations are inherent in the simulation process. For example, the high-velocity zone at 15-m depth and 10-m distances has different amplitudes in each simulation.

For attenuation tomography, the peak-to-peak amplitudes were also picked manually. The fitted covariance model is an anisotropic spherical model with a range of 9 m perpendicular to the holes and 3 m along the holes. The variance is 2 $(Np/m)^2$. We generated 128 simulations using the previously computed raypaths, and all of them reproduce the borehole logging data and the modeled covariances. Figure 7 shows the same four randomly selected numbers for attenuation simulations as were used for the slowness simulations in Figure 6. As is the case with slowness tomography, attenuation tomography simulations share the same main features except for a few local differences.

Petrophysical property reconstruction and full-waveform modeling

The 128 slowness and attenuation simulations were combined using relation 4, thus resulting in 128 conductivity and 128 permittivity fields. Figures 8 and 9 show four randomly selected conductivity and permittivity fields, respectively. As a first interpretation, both computed physical-property fields show a good visual agreement

with the modeled ones (Figures 3 and 4). Simple correlation (pixel by pixel) between the reference and computed conductivity and permittivity fields was calculated to measure the fit. Figures 10 comprises histograms of the simple correlation between each of the 128 computed conductivity (CS) fields and the reference field (Figure 10a) and between each of the computed permittivity (CK) fields, and
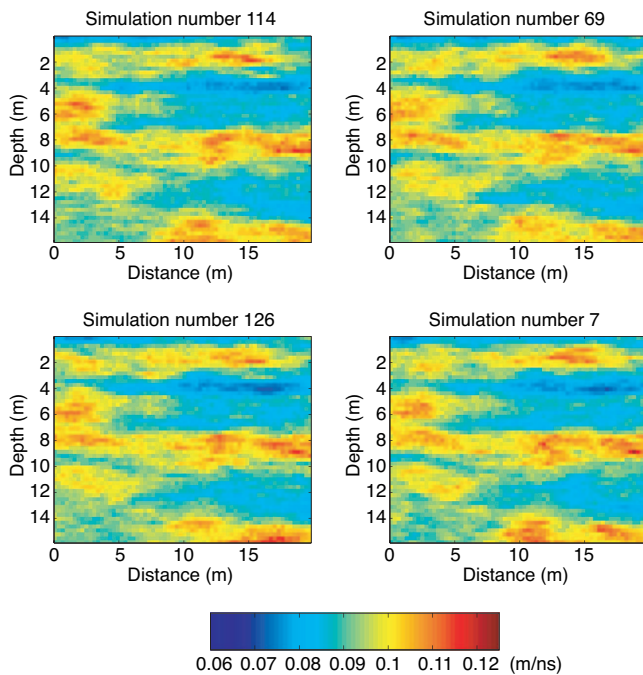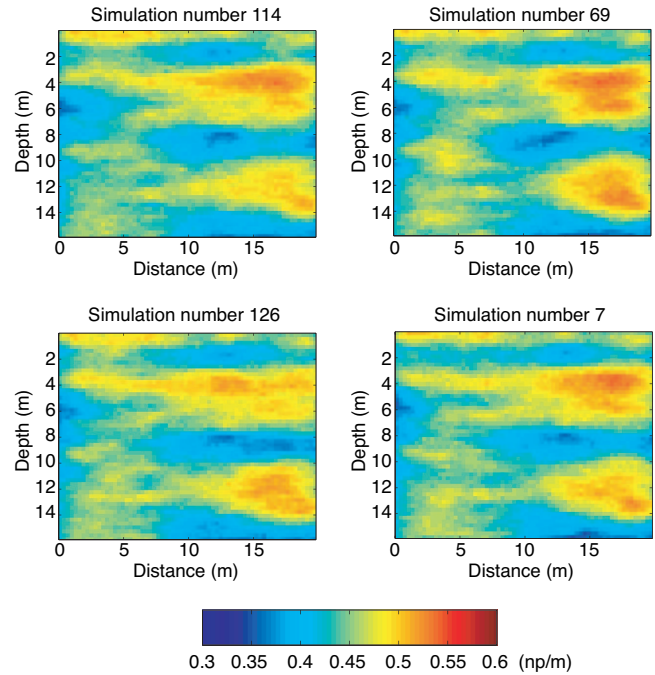

Figure 7. Same four randomly selected simulation numbers as in Figure 6, here for simulated attenuation fields.

Figure 6. Four randomly selected simulated velocity fields from the set of 128.
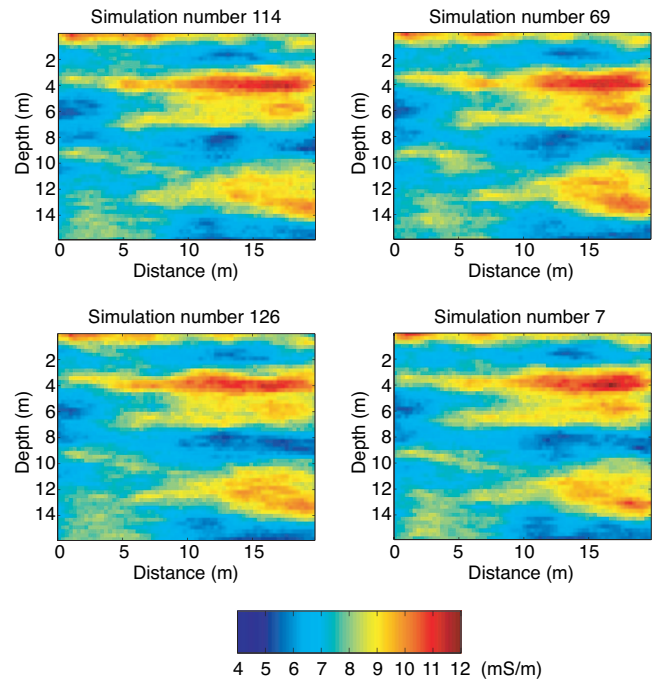

Figure 8. Reconstructed conductivity fields, using the same four randomly selected numbers as for the velocity and attenuation fields in Figures 6 and 7.

the reference field (Figure 10b). The overall mean and standard deviation of the permittivity simple correlation are 0.886 and 0.006, respectively, whereas the overall mean and standard deviation for the conductivity are 0.896 and 0.005, respectively. A higher correlation for conductivity arises because the permittivity is related to the square of the less accurate attenuation (relation 4). Even if the correlations are good, the interpretation is not obvious because the reference fields were first interpolated at the tomographic resolution. In addition, simple correlation only compares the pixel-to-pixel correlation, which does not imply any measure of the connectivity.

In a real experiment, the true physical-property fields are unknown and the simple correlation cannot be calculated. Moreover, all the simulated fields represent variations of maximum entropy around the same set of information, i.e., traveltimes, peak-to-peak amplitudes, logging data, and covariances. To differentiate the 128 simulated fields, new information is needed. In the ray-based method, time and first-cycle amplitude alone are used. Here, we propose to use the GPR-trace full-waveform modeling on the simulated fields to increase the level of information so we can select the best model. Therefore, full-waveform modeling is performed with each pair of conductivity-permittivity fields (interpolated to a grid of 1 by 1 cm), thereby yielding 128 sets of ten 10,000 traces (hereafter called the *simulated traces*). Generally, the transmitted wavelet is well reproduced and the secondary events also show a good agreement. For example, as shown in Figure 5, the secondary event at 127 ns (425 samples with 0.3 ns per sample) is well reproduced in terms of shape and amplitude.

To measure the trace-to-trace misfit, crosscorrelation is calculated between corresponding traces of each of the 128 simulated trace sets and the reference ones. For each trace, time shift and maximum correlation are computed. The mean of the absolute values of the time

shifts and the mean of the maximum correlation are calculated for each simulated trace set, leading to 128 values of time-shift misfit (TSM) and 128 values of amplitude misfit (AM). Figure 5 shows an example of a reference trace and a simulated trace with the same transmitter-receiver location. The shifted simulated trace that shows the maximum correlation with the reference trace also is shown in Figure 5. Figure 10c is the histogram of the mean of the absolute time shift for the 128 simulated trace sets. The overall mean of the time shift is ±3.2 samples (or 1 ns) with a standard deviation of 0.15. The averaged picked traveltime is 65 ns. Figure 10d is the histogram of the mean of the maximum correlation between pairs of shifted simulated traces and reference traces. The overall mean value is 0.93, with a standard deviation of 0.004. It shows that the simulated traces have a good fit with the reference ones, both in terms of correlation and time shift, thus confirming the quality of our conductivity and permittivity estimates.

The scatterplots of the TSM, AM, correlation between simulated-reference permittivity field (CK), and correlation between simulated-reference conductivity field (CS) are shown in Figure 11 to evaluate the relations between these parameters. Figure 11a shows the scatterplot between TSM and CK (the correlation is −0.4). Even
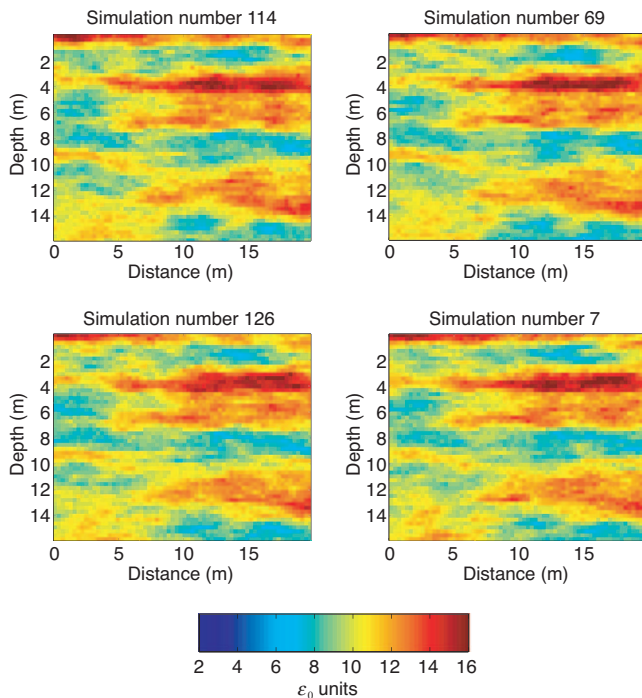

Figure 9. Reconstructed dielectric-constant fields, using the same four randomly selected numbers as for the velocity and attenuation fields in Figures 6 and 7.
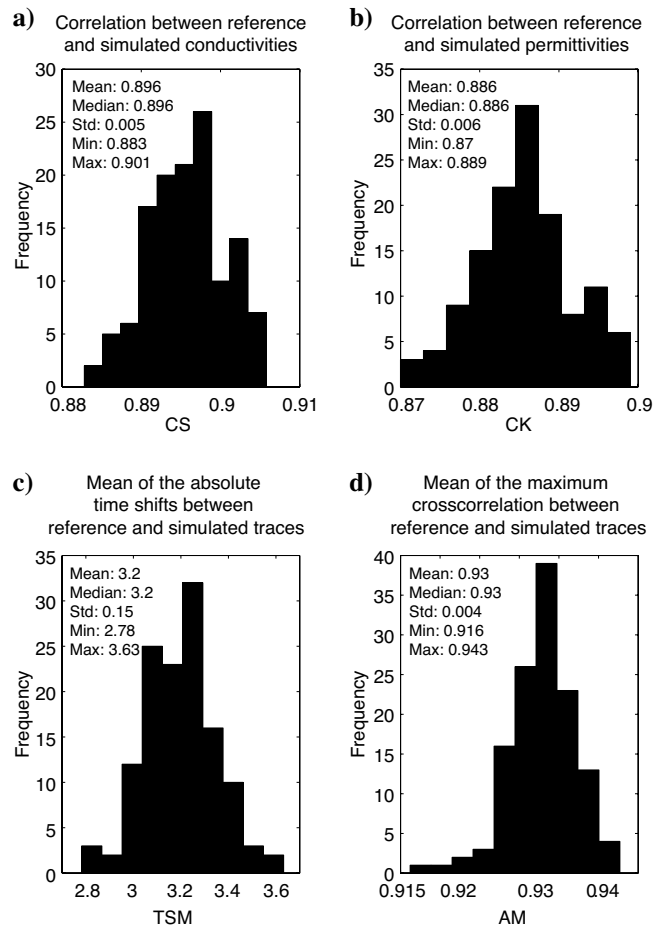

Figure 10. Histogram of (a) the correlation between the reference field and the 128 computed conductivity fields, (b) the correlation between the reference field and the 128 computed permittivity fields, (c) the average time shift between the reference traces and the computed traces, and (d) the mean of the maximum of the crosscorrelation between the reference traces and the measured traces.

though the correlation is not very high, Figure 11a shows that the computed permittivity fields associated with the smallest time shifts (TSM) better match the reference permittivity field. Figure 11c shows the scatterplot between AM and CK (the correlation is 0.6). Figure 11c shows that the computed conductivity fields associated with the highest maximum correlation (AM) better match the reference permittivity field. In addition, it also appears that the most poorly correlated permittivity field also corresponds to the set of simulated traces that has the worst fit to the reference traces. Figure 11b shows the scatterplot between TSM and CS (the correlation is −0.1), and Figure 11d shows the scatterplot between AM and CS (the correlation is 0.1). These low correlation factors indicate that, in our example, conductivity cannot be selected easily, as opposed to permittivity. However, even if correlation between AM and CS is poor, the computed traces that have the highest AM (with a maximum correlation greater than 0.94) are related to CS, showing a correlation above the mean of 0.896. This information makes it possible to discard the most poorly correlated conductivity fields.

Thus, the TSM and AM have a strong correlation with CK and a weaker correlation with CS. This means that full-waveform modeling helps in the selection of simulated fields with permittivity closer to the reference permittivity field. The small correlation with CS indicates that TSM and AM cannot be used to select simulated fields having a conductivity closer to the reference field (note, however, that all simulated fields have strong CK and CS values, which indicates that they are all strongly correlated to the reference field as a result of the conditioning of traveltime and amplitude data). The lack of sensitivity of TSM and AM in distinguishing the best simulated conductivity fields can be caused by many factors: loss of resolution because of the coarser tomography grid used to compute CS, insufficiency of the correlation coefficient to grasp the subtle differences between fields because it does not consider connectivity information, and weak intrinsic relations among TSM, AM, and CS. Addi-

tionally, the AM criteria might perform better for models with sharp conductivity contrasts, which yield stronger secondary arrivals. Further study is required on this subject.

CONCLUSIONS

Arrival times and amplitudes can be used to model slowness and attenuation covariance functions and then to geostatistically simulate slowness and attenuation fields. The simulated attenuation and slowness fields can be combined to obtain several permittivity and conductivity fields. That set of electric-property fields allows computation of as many pseudo-GPR-trace sets, thus showing the variability that can be expected from the survey geometry and the measured data. Our synthetic test case presented good raypath coverage and known slowness and attenuations at boreholes. As a result, all geostatistically simulated fields presented high correlations (above 0.88) with the reference field, as did the simulated traces with the reference traces (above 0.915). We showed that high trace correlations (AM) correspond to high permittivity correlations (CK) between simulated and reference fields. This result is important in real applications because only the traces are available. Thus, it is possible to select more realistic permittivity fields by maximizing the match between simulated traces and reference (or observed) traces, following our approach. On the other hand, we found no significant link between the traces match and the conductivity-fields match.
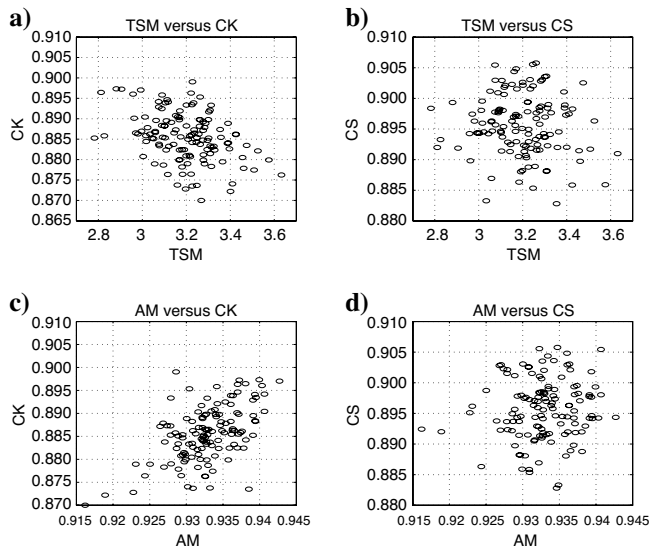
Figure 11. Scatterplots of (a) TSM versus CK, (b) TSM versus CS, (c) AM versus CK, and (d) AM versus CS, where TSM is time-shift misfit, AM is the amplitude misfit, CK is the correlation between simulated and synthetic permittivity fields, and CS is the correlation between simulated and synthetic conductivity fields.

REFERENCES

Alumbaugh, D. L., and G. A. Newman, 2000, Image appraisal for 2D and 3D EM inversion: Geophysics, **65**, 1455–1467.
Asli, M., D. Marcotte, and M. Chouteau, 2000, Direct inversion of gravity data by cokriging: Presented at the 6th International Geostatistical Congress.
Balanis, C. A., 1989, Advanced engineering electromagnetics: John Wiley & Son.
Bellefleur, G., M. Chouteau, and P. Sénéchal, 2000, Potentials pitfalls for amplitude inversion revealed by overlapping radar surveys: Proceedings of the 8th International Conference on Ground-penetrating Radar: SPIE, 126–131.
Berryman, J. G., 1991, Lecture notes on nonlinear inversion and tomography: Borehole seismic tomography, Earth Resources Laboratory, MIT.
Cai, W., F. Qin, and G. T. Schuster, 1996, Electromagnetic velocity inversion using 2-D Maxwell's equations: Geophysics, **61**, 1007–1021.
Carcione, J. M., and M. A. Schoenberg, 2000, 3-D ground-penetrating radar simulation and plane-wave theory in anisotropic media: Geophysics, **65**, 1527–1541.
Chew, W. C, J. M. Jin, and E. Michelssen, 1997, Complex coordinate stretching as a generalized absorbing boundary condition: Microwave Optical Technology Letters, **15**, 363–369.
Chilès, J-P., and P. Delfiner, 1999, Geostatistics, modelling spatial uncertainty: Wiley Series on Probability and Statistics, John Wiley & Son.
Day-Lewis, F. D., K. Singha, and A. M. Binley, 2005, Applying petro-physical models to radar travel time and electric resistivity tomograms: Resolution-dependent limitations: Journal of Geophysical Research, **110**, B0826.
Franklin, J. N., 1970, Well-posed stochastic extensions of ill-posed linear problems: Journal of Mathematical Analytical Application, **31**, 682–716.
Giroux B., and M. Chouteau, 2006, On the processing of borehole georadar data for ray-based attenuation tomography GPR 2006: *in* J. Daniels and C.-C. Chen, eds., Proceedings of the Eleventh International Conference on Ground-Penetrating Radar.

Giroux, B., E. Gloaguen, and M. Chouteau, 2007, bh_tomo — A Matlab borehole georadar 2D tomography package: Computers and Geosciences, **33**, 126–137.

Gloaguen, E., M. Chouteau, and D. Marcotte, 2003, Borehole velocity tomography with velocity constraints along holes using slowness covariance estimation and cokriging: Rundtisch gesprach, 35–39.

Gloaguen, E., M. Chouteau, D. Marcotte, and R. Chapuis, 2001, Estimation of hydraulic conductivity of an unconfined aquifer using cokriging of GPR and hydrostratigraphical data: Journal of Applied Geophysics, **47**, 135–152.

Gloaguen, E., D. Marcotte, M. Chouteau, and H. Perroud, 2005, Borehole radar velocity inversion using cokriging and cosimulation: Journal of Applied Geophysics, **57**, 242–259.

Hollender, F., 1999, Interprétation de la distorsion des signaux géoradar propagés et réfléchis: Ph.D. thesis, Institut National Polytechnique de Grenoble (INPG).

Holliger, K., and T. Bergmann, 2002, Numerical modeling of borehole georadar data: Geophysics, **67**, 1249–1257.

Hyndman, D., and J. Tronicke, 2005, Hydrogeophysical studies at the local scale: The saturated zone, *in* V. P. Singh, Y. Rubin, and S. S. Hubbard, eds., Hydrogeophysics: Water Science and Technology Library 50, Springer-Verlag New York, Inc., 391–412.

Kitanidis, P. K., 1995, Quasi-linear geostatistical theory for inversing: Water Resources Research, **31**, 2511–2519.

Lane, J. W., P. K. Koesten, F. P. Haeni, M. Vendl, and D. Yeskis, 1998, Use of borehole radar methods to monitor the movement of a saline tracer in carbonate rock at Belvidere, Illinois: Proceedings of the Symposium on the Application of Geophysics to Engineering and Environmental Problems.

Le Ravalec, M., B. Noetinger, and L. Y. Hu, 2000, The FFT moving average generator: An efficient numerical method for generating and conditioning Gaussian simulations: Mathematical Geology, **32**, 701–723.

Lesmes, D. P., and S. P. Friedman, 2005, Relationships between the electric and hydrogeophysical properties of rocks and soils, *in* V. P. Singh, Y. Rubin, and S. S. Hubbard, eds., Hydrogeophysics: Water Science and Technology Library 50, Springer-Verlag New York, Inc., 87–128.

Luo, Y., and G. T. Schuster, 1991, Wave-equation traveltime inversion: Geophysics, **56**, 645–653.

Topp, G. C., J. L. Davis, and A. P. Annan, 1980, Electromagnetic determination of soil water content: Measurements in coaxial transmission lines: Water Resources Research, **16**, 574–582.

Tronicke, J., P. Dietrich, U. Wahlig, and E. Apel, 2002, Integrating surface georadar and crosshole radar tomography: A validation experiment in a braided stream deposit: Geophysics, **67**, 1495–1504.

Tronicke, J., K. Holliger, W. Barrash, and M. D. Knoll, 2004, Multivariate analysis of cross-hole georadar velocity and attenuation tomograms for aquifer zonation: Water Resources Research, **40**, W01519 http://dx-.doi.org/ , doi: 10.1029/2003WR002031.

Vasco, D. W., J. E. Peterson, and K. H. Lee, 1997, Ground-penetrating radar velocity tomography in heterogeneous and anisotropic media: Geophysics, **62**, 1758–1773.

Yilmaz, O., 2001, Seismic data analysis: SEG.

Zhou, B., and P. K. Fullagar, 2001, Delineation of sulfide ore-zones by borehole radar tomography at Hellyer mine, Australia: Journal of Applied Geophysics, **47**, 261–269.